

Inverse Orbital Torque via Spin-Orbital Entangled States

E. Santos¹, J. E. Abrão¹, Dongwook Go^{2,3}, L. K. de Assis⁴, Yuriy Mokrousov^{2,3}, J.B.S. Mendes⁵,
and A. Azevedo¹

¹ *Departamento de Física, Universidade Federal de Pernambuco, Recife, Pernambuco 50670-901, Brasil.*

² *Peter Grünberg Institut and Institute for Advanced Simulation, Forschungszentrum Jülich and JARA, 52425 Jülich, Germany.*

³ *Institute of Physics, Johannes Gutenberg University Mainz, 55099 Mainz, Germany.*

⁴ *Universidade Federal de Pernambuco, Programa de Pós-Graduação em Ciências dos Materiais, Recife, Pernambuco 50740-560, Brasil.*

⁵ *Departamento de Física, Universidade Federal de Viçosa, 36570-900 Viçosa, Minas Gerais, Brazil.*

While current-induced torque by orbital current has been experimentally found in various structures, evidence for its reciprocity has been missing so far. Here, we report experimental evidence of strong inverse orbital torque in YIG/Pt/CuO_x (YIG = Y₃Fe₅O₁₂) mediated by spin-orbital entangled electronic states in Pt. By injecting spin current from YIG to Pt by the spin pumping via ferromagnetic resonance and by the spin Seebeck effect, we find a pronounced inverse spin Hall effect-like signal. While a part of the signal is explained as due to the inverse spin-orbital Hall effect in Pt, we also find substantial increase of the signal in YIG/Pt/CuO_x structures compared to the signal in YIG/Pt. We attribute this to the inverse orbital Rashba-Edelstein effect at Pt/CuO_x interface mediated by the spin-orbital entangled states in Pt. Our work paves the way toward understanding of spin-orbital entangled physics in nonequilibrium and provides a way for electrical detection of the orbital current in orbitronic device applications.

In the age of information technology, spin-based electronics has found wide application in data storage and processing. This field is facing increasing challenges that demand increasingly efficient materials for generation and manipulation of spin currents [1, 2]. It turned out that spin-orbit coupling (SOC) enables generation of nonequilibrium spin accumulation, e.g. by spin Hall effect (SHE) [3-5] and Rashba-Edelstein effect [6-9]. A reciprocal effect such as inverse SHE (ISHE) provides a way to detect the spin in an electrical way. Injection of the SOC-induced spin to a ferromagnet can exert torque on the magnetization, which is known as spin-orbit torque (SOT), an effect that originates from the exchange interaction between non-equilibrium spins and local magnetic moments [10-12]. Since SOC increases with the atomic number, heavy metals such as Pt, Ta and W have been widely used in spintronics investigation, making them prime candidates for devices used to manipulate the magnetization by electrical means only. In this scenario, light materials such as Cu are often overlooked, because they have negligible SOC.

However, recent studies have shown that naturally oxidized Cu films can significantly enhance SOT efficiency, which reveals a crucial role of an oxide interface [13-16]. This effect can be explained in the newly developed framework of orbital angular momentum (OAM) currents, which can be generated even in weak SOC materials. Apparently, OAM would not play any important role due to the angular momentum quenching in solids, however, it has been shown that the orbital Hall effect (OHE) can generate an OAM current in a transverse direction to an external electric field even if the OAM is completely quenched in the ground state [17-21]. At surfaces and interfaces, where the inversion symmetry is broken, orbital hybridizations induce a local electric dipole which influences the OAM polarization. Its interaction with structural asymmetry results in the orbital Rashba effect (ORE) [22-27], which induces a chiral OAM texture for electronic states in \mathbf{k} -space. Thus, application of an external electric field can result in nonequilibrium OAM accumulation, which is known as the orbital Rashba-Edelstein effect (OREE) [27-28] – the orbital counterpart of the spin Rashba-Edelstein effect [6-8]. Since the orbital carries angular momentum, transfer of the OAM to the magnetization of a magnetic material provides an alternative mechanism to induce magnetization dynamics [29]. Such orbital torques (OTs) provide a promising route for magnetic nanodevices based on light elements.

Among different material candidates, a surface-oxidized Cu (CuO_x) is found to exhibit a strong OREE [27]. This is supported by recent papers on OT in heterostructures

involving CuO_x [27, 29, 30]. In particular, Ref. [29] demonstrated a novel route to achieve large torque efficiency using strong SOC of Pt in TIG/Pt/ CuO_x structure, where TIG = $\text{Tm}_3\text{Fe}_5\text{O}_{12}$. In Ref. [29], the OAM induced by the OREE is harnessed by the orbital-to-spin conversion in Pt which has strong SOC, and the resulting spin exerts torque on the magnetization of TIG. So far, we emphasize that there is still no experimental evidence of its reciprocal process, the inverse OT. We also note that Refs. [16,31] found negligible efficiency for the inverse OT.

In this Letter, we report an experimental observation of the inverse OT in heterostructures of YIG(40)/Pt(t_{Pt})/ CuO_x (3) by means of spin pumping via ferromagnetic resonance (FMR) and longitudinal spin Seebeck effect (LSSE) in YIG, where the numbers in parentheses indicate the thickness of each layer in nanometers. When comparing with the result in YIG(40)/Pt(t_{Pt}), we find substantial increase of the inverse SHE-like signal upon adding a CuO_x capping layer, suggesting a crucial role of Pt/ CuO_x interface, where strong ORE exists. From this, we conclude that upon spin injection, nonequilibrium electronic states exhibit strong entanglement between the spin and orbital due to the strong SOC of Pt, and it is converted into charge current by the inverse OREE (IOREE) at Pt/ CuO_x interface. The efficiency of this process depends on two aspects: (1) the spin-orbital degree of entanglement that determines how efficiently the orbital current is conducted upward; (2) how strong is the IOREE, which is driven by the perpendicular E-field (due to the inversion symmetry breaking and/or any charge transfer process due to the oxidation) at the Pt/ CuO_x interface. Figure 1 presents a schematic illustration of the mechanism for converting spin-orbital entangled current into charge current by two mechanisms. The spin is injected from YIG and as the spin entangles with the OAM at Pt, it is converted into a charge current not only by the inverse SHE-OHE in Pt [Fig. 1(a)] but also via the IOREE at the CuO_x interface [Figs. 1(b,c)]. We find that this contribution is much stronger than the “conventional” contribution by the ISHE in Pt. Our finding not only demonstrates the inverse OT unambiguously, but also sheds lights on the nonequilibrium spin-orbit physics. The YIG(40) film used in this work was grown by liquid phase epitaxy onto a 0.5 mm thick (111)-oriented $\text{Gd}_3\text{Ga}_5\text{O}_{12}$ (GGG). The Pt and Cu films were DC-sputter-deposited at room temperature in a working pressure of 2.8 mTorr and a base pressure of 2.0×10^{-7} Torr or lower. The set of samples with the Cu capping layer was left outside the chamber for two days to naturally oxidize. All the YIG samples were cut from the same YIG(40) film in pieces with lateral dimensions of 1.5 x 3.0 mm² (see Ref. [32] for details).

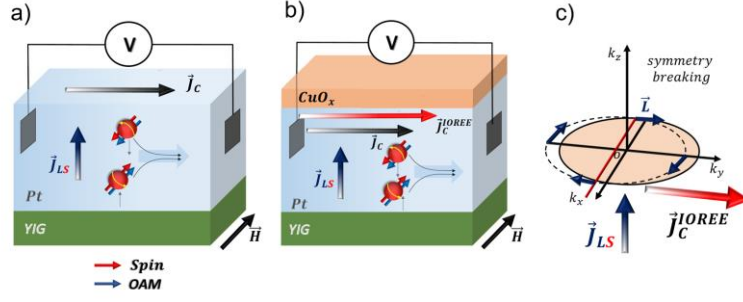


Fig. 1. Illustration of the inverse SHE-OHE process. a) Without CuO_x layer, the only contribution is due to the conversion of J_{LS} in charge current. b) With CuO_x layer, the additional J_C^{IOREE} appears driven by the interface Pt/ CuO_x . c) IOREE in the presence of a chiral OAM texture in \mathbf{k} -space.

The investigation of the structural properties of the heterostructures was carried out by conventional X-ray diffraction (XRD), grazing incidence X-ray diffraction (GIXRD), and scanning electron microscopy (SEM) images. To investigate the oxidation process, we deposited a thick film of Cu(60) on top of the Pt(3) layer and left the sample exposed to air. The GIXRD pattern in Fig. 2(a) clearly shows the diffraction peaks characteristic of CuO_x and of the polycrystalline Cu film with preferential texture oriented along the planes (111), (200), (220) and (202), as previously reported [33]. We deposited a capping layer of Pt(5) on the Cu surface and the GIXRD pattern is shown in Fig. 2(b) where no CuO_x peaks were identified. Clearly the capping layer of Pt(5) prevents the Cu oxidation. The XRD spectrum also shows the peak corresponding to (111) Bragg reflections from the Cu film, demonstrating that the orientation of the GGG substrate strongly influences the orientation of the Cu grains. Figures 2(c,d) show SEM images of Cu/ CuO_x films deposited in GGG (111)/Pt(3) revealing a continuous film with different shapes of CuO_x pyramids with dimensions smaller than $1 \mu\text{m}$ associated to the orientation of the GGG substrate.

We used FMR-driven spin-pumping (FMR-SP) technique excited at 9.41 GHz [34, 35] to investigate the interplay between orbital and spin currents in two series of heterostructures: YIG(40)/Pt(t_{Pt}) and YIG(40)/Pt(t_{Pt})/ $\text{CuO}_x(3)$, where $0 \leq t_{\text{Pt}} \leq 7 \text{ nm}$. For the second series of samples, a Cu(3nm) island with dimensions $1.5 \times 2.0 \text{ nm}^2$ was deposited on top of the Pt layer. In this technique, illustrated in Fig. 3(a), a spin current is coherently injected through the YIG/Pt interface by the uniform precession of the YIG magnetization under FMR. The upward spin current density (J_S^{SP}), diffuses through the Pt layer generating a local electric field, $E_{\text{ISHE}} \propto j_S^{\text{SP}} \times \sigma$, by means of the ISHE, where spin

current polarization $\sigma \parallel \mathbf{M}_{\text{YIG}}$. By measuring the voltage difference (V_{SP}) produced between the two electrodes, we can define the SP signal as the current $I_{\text{SP}} = V_{\text{SP}}/R$, where R is the electric resistance along the Pt layer. Figure 3(b) shows typical I_{SP} signals for the sample YIG/Pt(2)CuO_x(3), which obey the equation $\mathbf{J}_C^{\text{SP}} = (2e/\hbar)\theta_{\text{SH}}(\mathbf{J}_S^{\text{SP}} \times \boldsymbol{\sigma})$ as expected, i.e., null at $\varphi = 90^\circ$ (black), maximum positive at $\varphi = 0^\circ$ (blue) and maximum negative $\varphi = 180^\circ$ (red). Here φ is the angle between the DC field and the direction of the voltage measurement. Inset of Fig. 3(b) shows the same behavior obtained for the sample YIG(40)/Pt(2). Figure 3(c) clearly shows the significant gain of the SP signal, for the sample YIG(40)/Pt(2)/CuO_x(3) (black) compared with the sample YIG(40)/Pt(2) (red).

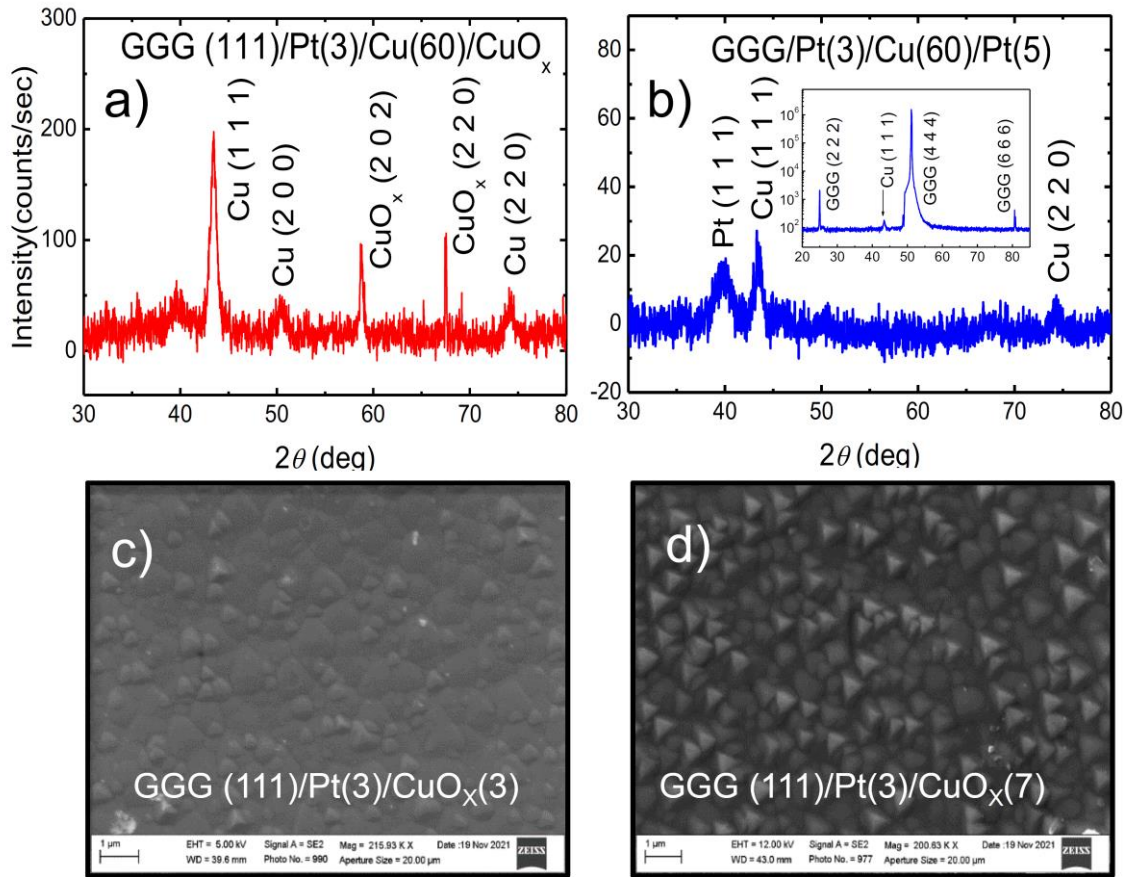


Fig. 2. a) Shows the GIXRD pattern of a film of Cu(60) that was left in contact with air for two days. The result shows the presence of strong CuO_x peaks. In b), the GIXRD pattern clearly shows that a capping layer of Pt(5) prevents the Cu layer oxidation. Figs. c) and d) show SEM surface images of CuO_x(3) and CuO_x(7), respectively. The images reveal pyramidal structures associated to the orientation of the GGG substrate. Inset of b) shows the conventional XRD pattern of GGG/Pt(3)/Cu(60)/CuO_x, exhibiting reflections associated with the (222), (444) and (666) crystal planes of GGG as well as (111) texture of the Cu layer.

While the bare YIG presented an FMR linewidth of $\Delta H = 2.63$ Oe, it increases to 2.84 Oe after deposition of Pt and increases for 3.06 Oe after deposition of CuO_x on top of Pt, which characterizes the transfer of spin angular moment from YIG to the Pt layer (inset of Fig. 3(c)). To confirm the effect of the Cu oxidation, we prepared a sample in which the Cu layer is protected by a layer of MgO(5). The results of Fig. 3(d), shows that the I_{SP} signals for the samples YIG(40)/Pt(2)/Cu(3)/MgO(5) (blue) and YIG(40)/Pt(2) (red), are equivalent, thus confirming that the enhancement shown in Fig. 3(c) comes from the Pt(2)/ CuO_x (3) interface. Figure 3(e) shows the dependence of the peak value of I_{SP} , as a function of the rf power used to excite the FMR, for both samples [32]. By comparing the slopes of the black and red lines, we observed that the gain in I_{SP} , due to the presence of CuO_x (3), is around 5 times. The dependence of I_{SP} as a function of the Pt layer thickness, with a rf power of 110mW, for both set of samples is shown in Fig. 3(f). The I_{SP} signal for the sample YIG(40)/Pt(t_{Pt}) (red) exhibits the usual behavior, i.e., increases as the t_{Pt} increases reaching the saturation for $t_{\text{Pt}} > 4$ nm. On the other hand, the dependence of I_{SP} on t_{Pt} for the set of samples with a capping layer of CuO_x (3) (black), increases sharply reaching a maximum at $t_{\text{Pt}} \sim 3$ nm, then decreases to the same range of saturation values observed for the YIG(40)/Pt(t_{Pt}) samples. The solid lines in Fig. 3(f) are guide to the eyes. The unusual dependence of I_{SP} on t_{Pt} , for the samples YIG(40)/Pt(t_{Pt})/ CuO_x (3), is explained as due to the interplay between the spin and orbital states that is mediated by the strong SOC of Pt. The spin-orbital entangled current (J_{LS}) is partially converted into charge current by means of the inverse spin and orbital Hall effects of Pt and by the strong IOREE at the Pt/ CuO_x interface. As the Pt layer thickness increases, the J_{LS} current no longer reaches the Pt/ CuO_x interface due to the finite diffusion length of the spin-orbital entangled current in Pt, thus causing the measured voltage to decrease.

To confirm the results obtained by SP, we performed spin injection measurements using the LSSE technique on the same two sets of samples. In LSSE, the application of a temperature gradient in a magnetic material generates a spin current along the direction of the temperature gradient, which is the magnetic analog of the thermoelectric Seebeck effect [36]. Figure 4(a) shows schematically the LSSE setup, in which a thermal gradient is applied perpendicular to the sample plane [32]. It highlights the perpendicular temperature gradient ∇T and the upward spin-orbital entangled current (J_{LS}), the ISHE-

like charge currents in Pt (J_C) due to the inverse spin and orbital Hall effects, as well as the OREE current on the Pt/CuO_x interface.

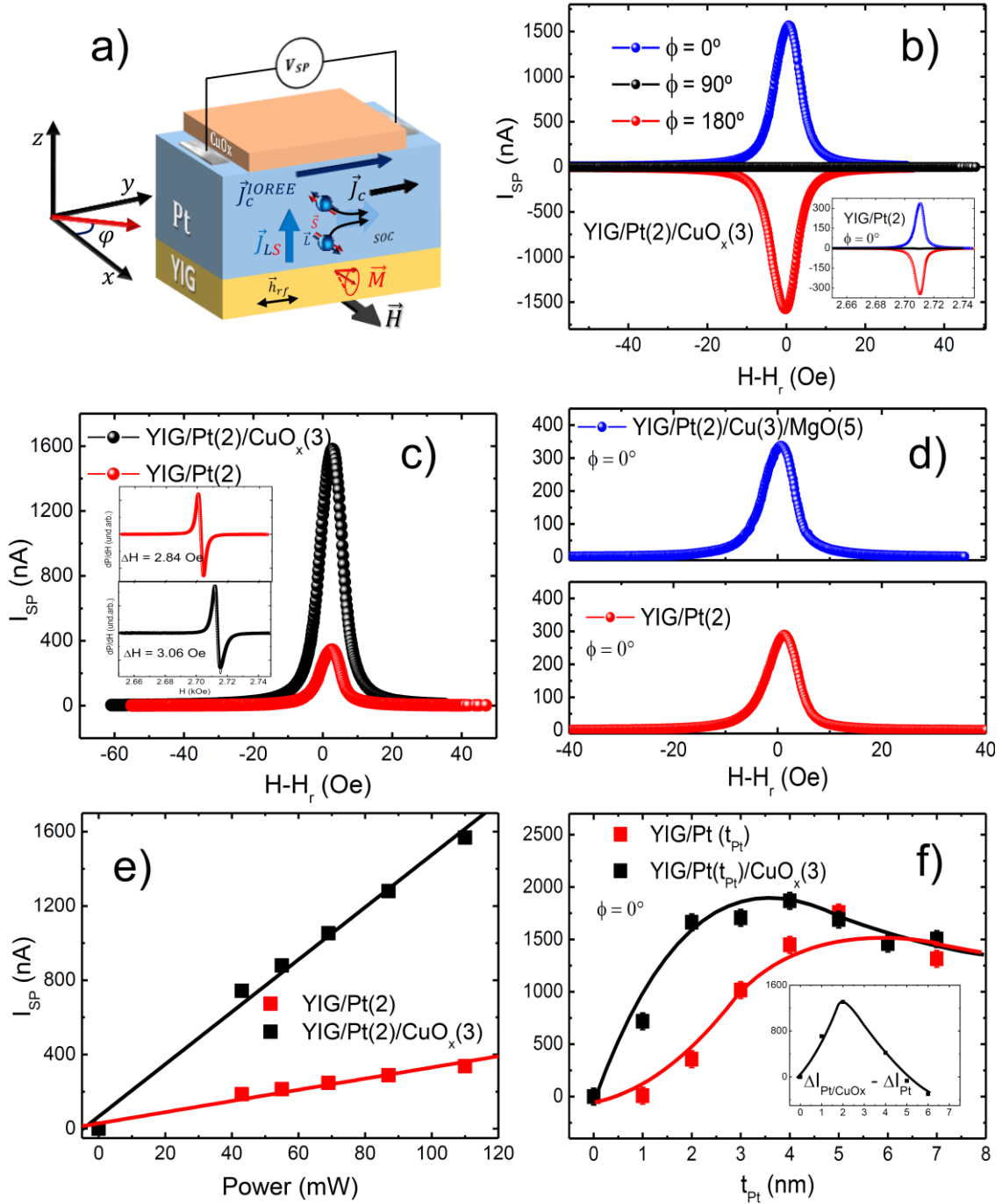


Fig. 3 - a) Schematically shows the SP configuration. b) Shows the typical I_{SP} signals for the samples with and without the CuO_x cover layer (inset). c) Shows the comparison of the SP signals of the samples with (black) and without (red) CuO_x capping layer, respectively, obtained for $P_{rf} = 110$ mW. The inset shows the derivative of the FMR absorption signal for both samples. d) Shows I_{SP} signals for the samples YIG(40)/Pt(2)/Cu(3)/MgO(5) (blue) and YIG/Pt(2) (red), which confirm that the enhancement occurs only when the Cu cover layer is oxidized. e) Shows the dependence of I_{SP} signals, as a function of the rf power, for the samples YIG/Pt(2) (red) and YIG/Pt(2)/CuO_x(3) (black). f) Shows the dependence of I_{SP} as a function of t_{Pt} , for the samples YIG/Pt(2) (red) and YIG/Pt(2)/CuO_x(3) (black). The solid lines are guide to the eyes. The inset shows the difference between the data of the samples with and without the CuO_x cover layer, which reaches a maximum for $t_{Pt} \approx 2$ nm.

Figure 4(b) shows LSSE signals, where thermal voltages (V_{LSSE}) are measured along sample plane for heterostructures of YIG(40)/Pt(2) (red) and YIG(40)/Pt(2)/CuO_x(3) (black). From negative to positive field sweep, the perpendicular temperature gradient is fixed at the same value for the measurements of both samples. Surprisingly, the measured LSSE signal value for the sample with a CuO_x capping layer increased more than two times compared to the sample without CuO_x. Figure 4(c) shows the LSSE signals of YIG(40)/Pt(2)/CuO_x(3) for various temperature differences ($0\text{K} \leq \Delta T \leq 20\text{K}$) between the heat baths placed on the lower and upper surfaces of the sample [32]. The LSSE signal amplitude (ΔI_{LSSE}), defined in Fig. 4(b), increases linearly as a function of ΔT , as summarized in Fig. 4(d) for the heterostructures of YIG(40)/Pt(2)/CuO_x(3) (black) and YIG(40)/Pt(2) (red), respectively. The linear fits of Fig. 4(d) were obtained by means of $\Delta I_{\text{LSSE}} = -\alpha_{\text{FM}}\Delta T \cos \varphi$, where $\alpha_{\text{FM}} = \frac{S_{\text{FM}}}{R} \left(\frac{w_{\text{Pt}}}{t_{\text{YIG}} + t_{\text{GGG}}} \right)$ [37, 38]. Here, S_{FM} is the spin-Seebeck coefficient, w_{Pt} is the distance between the electrical contacts, φ is the azimuthal angle as defined in Fig. 4(a), and t_{YIG} and t_{GGG} are the thicknesses of the YIG and GGG layers, respectively [32]. From the linear fits shown in Fig. 4(d) we obtained $\alpha_{\text{FM}}^{(1)}/\alpha_{\text{FM}}^{(2)} \cong 2.6$, where $\alpha_{\text{FM}}^{(1)}$ and $\alpha_{\text{FM}}^{(2)}$ are the linear coefficients for the black and red lines, respectively. Thus, the presence of CuO_x increased the LSSE signal by a factor of 2.6. Figures 4(e,f) show the dependence of ΔI_{LSSE} for both series of samples as a function of t_{Pt} for $\Delta T = 27\text{K}$ and $\Delta T = 3\text{K}$, respectively. As expected, the dependence of $\Delta I_{\text{LSSE}} \times t_{\text{Pt}}$ for YIG(40)/Pt(t_{Pt}) is given by $\Delta I_{\text{LSSE}} = \beta \lambda_{\text{N}} \tanh(t_{\text{Pt}}/2\lambda_{\text{N}})$, where β depends on the interface YIG/Pt properties and λ_{N} is the spin diffusion length in the Pt layer [32,37]. ΔI_{LSSE} increases monotonically, reaching the saturation for $t_{\text{Pt}} > 4\text{nm}$, and the red line corresponds to the best fit to the data with $\lambda_{\text{N}} = 1.6 \pm 0.2\text{nm}$, which is in the range of reported spin diffusion lengths for Pt that span an order of magnitude, ranging from just over 1 nm to 10 nm [35, 39]. On the other hand, the results for the samples YIG(40)/Pt(t_{Pt})/CuO_x(3), indicated in Figs. 4(e,f) by the black symbols, shows the same behavior of the SP signal of Fig. 3(f). Black lines are guide to the eyes. The LSSE signal rapidly increases as a function of t_{Pt} , reaches a maximum for $t_{\text{Pt}} \approx 3\text{nm}$ and then decreases to values of the same order as the saturation values obtained for the YIG(40)/Pt(t_{Pt}) samples.

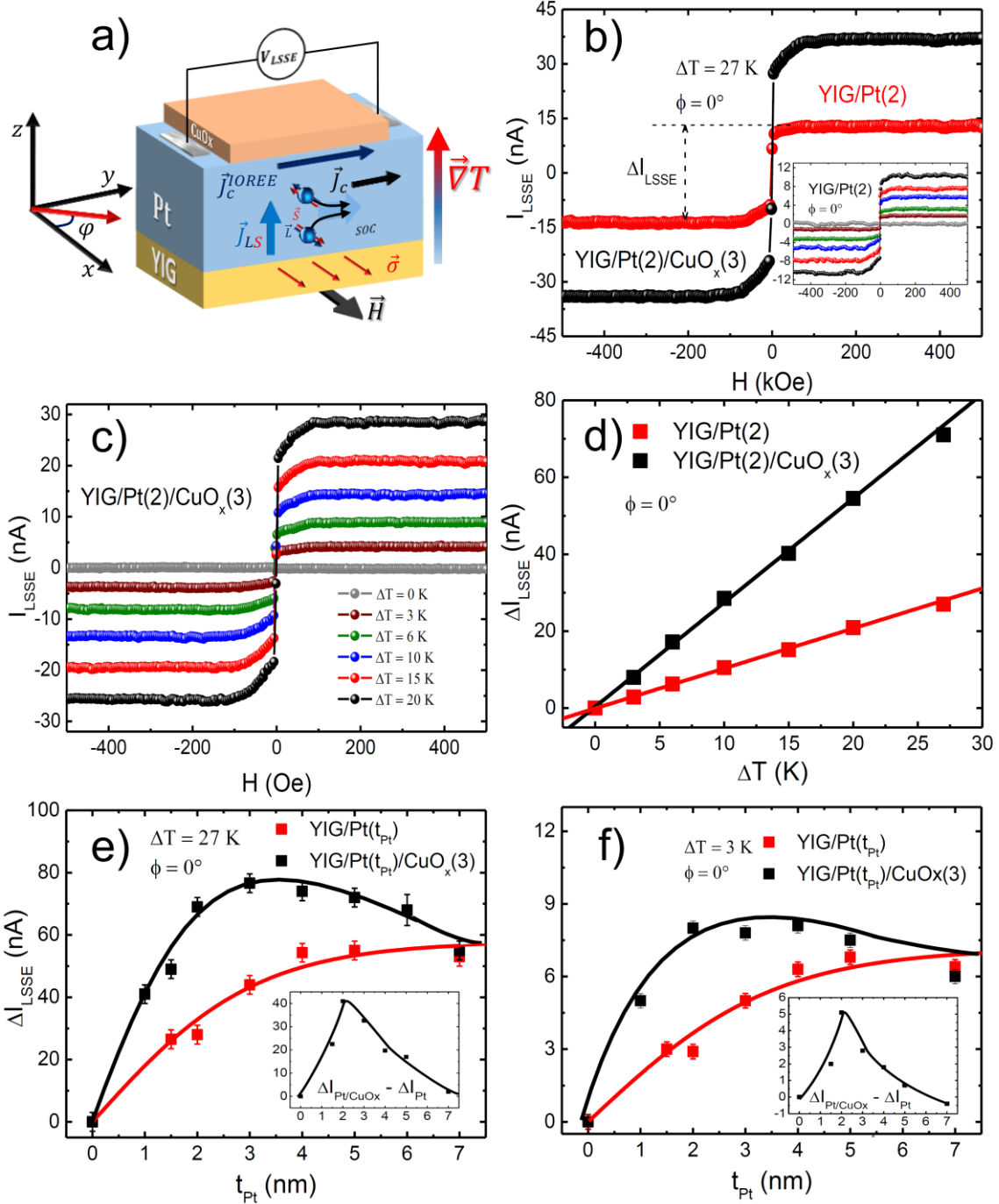


Fig. 4 - a) Schematically shows the LSSE configuration. b) Shows the field sweep of the LSSE signal for the samples with (black) and without (red) a capping layer of CuO_x(3), for $\Delta T = 27$ K. With the deposition of the CuO_x layer, the LSSE signal obtained a gain of order 2.6. c) Shows the field scans curves for values of ΔT ranging from 0K to 20K, for the sample with the cover layer of CuO_x. The inset of 4 b) shows the same curves obtained for the sample YIG(40)/Pt(2). d) Shows the dependence of ΔI_{LSSE} as a function of ΔT for the samples YIG/Pt(2)/CuO_x(3) (black) and YIG/Pt(2) (red), where ΔI_{LSSE} is defined in b). Figs. 4 e) and f) show the dependence of ΔI_{LSSE} as a function of t_{Pt} for $\Delta T = 27$ K and $\Delta T = 3$ K, respectively. The red symbols are the data for the sample YIG/Pt(t_{Pt}) and the black symbols are the data for the sample with the capping layer of CuO_x. The insets of Figs. 4 e) and f) shows the difference between the data of the samples with and without the CuO_x cover layer, which reaches a maximum for $t_{Pt} \approx 2$ nm.

This very peculiar behavior can also be explained as due to the interplay between the electron spin and orbital degrees of freedom. In the LSSE, an upward spin current, $\mathbf{J}_S^{\text{LSSE}} \parallel \nabla_z T$, driven by the $\nabla_z T$, is injected through the YIG/Pt interface. Due to the strong SOC of Pt, the out-of-equilibrium spin states, thermally pumped into Pt, give rise to a spin-orbital entangled current (\mathbf{J}_{LS}). As the entangled spin-orbital current propagates upward through the Pt layer, it is converted into charge current, either by the inverse SHE or inverse OHE, as well as by the strong OREE at the Pt/CuO_x interface. It is important to mention that preliminary results performed in YIG/Pt(4)/AlO_x(3) also exhibited a gain of more than twice compared to YIG/Pt(4) (See Fig. S4 in the Supplemental Material).

The interaction between charge, spin, and orbital degrees of freedom, triggered by the FMR-driven or thermal-driven spin pumping, represents a unifying principle to explain the experimental results reported in this work. By injecting the pure spin current from the FMR-SP or LSSE from YIG into Pt, the nonequilibrium electronic states have strong entanglement between the spin and orbital and carries spin-orbital entangled current. In Pt, a part of the spin-orbital entangled current is converted into charge current. This occurs either by the inverse SHE or inverse OHE. We note that this has been conventionally interpreted solely in terms of the inverse SHE, neglecting the orbital contribution. Meanwhile, as the spin-orbital entangled current propagates across the Pt layer and reaches the CuO_x interface, it is converted to charge current via the inverse OREE. However, if the Pt layer is thicker than the relaxation length for the spin-orbital entangled current, it cannot reach the CuO_x interface and only the inverse SHE/OHE contribution contributes. This explains why the efficiencies for YIG/Pt and YIG/Pt/CuO_x converge to the same value for $t_{\text{Pt}} > 7\text{nm}$.

In conclusion, we used LSSE and FMF-SP techniques to investigate the interplay between spin, orbital and charge degrees of freedom in heterostructures of YIG(40)/Pt(t_{Pt})/CuO_x(3). Due to the strong SOC of Pt, the spin states, pumped through the YIG/Pt interface, entangle with the local orbital states, thus generating an upward pure spin-orbital current (\mathbf{J}_{LS}) without flow of charge. Part of this current is converted, within the Pt, into a transverse charge current by either the inverse-SHE effect or the inverse-OHE effect. Part of the remaining spin-orbital current that flows upward, is transformed into a transverse charge current by means of the inverse OREE. This current is added to the previous charge current, thus increasing the resulting charge current. The dependence of the charge current as a function of Pt layer thickness, provides a clear picture of the phenomenon of converting spin-orbital current to charge current. As the Pt layer thickness

becomes larger than the spin-orbital diffusion length, the J_{LS} no longer reaches the Pt/CuO_x interface, and the IOREE mechanism ceases to occur. Therefore, the charge current value is reduced to the saturation values of the charge currents generated only by the inverse SHE combined with the inverse OHE. Certainly, the results reported here open new avenues to understand the basic mechanisms underlying the spin-orbital entanglement phenomena.

Acknowledgements

This research was supported by Conselho Nacional de Desenvolvimento Científico e Tecnológico (CNPq), Coordenação de Aperfeiçoamento de Pessoal de Nível Superior (CAPES), Financiadora de Estudos e Projetos (FINEP), Fundação de Amparo à Ciência e Tecnologia do Estado de Pernambuco (FACEPE), Universidade Federal de Pernambuco, Fundação de Amparo à Pesquisa do Estado de Minas Gerais (FAPEMIG) - Rede de Pesquisa em Materiais 2D and Rede de Nanomagnetismo.

References

- [1] B. Dieny; I. L. Prejbeanu; K. Garello; P. Gambardella; P. Freitas; R. Lehndorff; W. Raberg; U. Ebels; S. O. Demokritov; J. Akerman; A. Deac; P. Pirro; C. Adelman; A. Anane; A. V. Chumak; A. Hirohata; S. Mangin; Sergio O. Valenzuela; M. Cengiz Onbaşlı; M. d'Aquino; G. Prenat; G. Finocchio; L. Lopez-Diaz; R. Chantrell; O. Chubykalo-Fesenko, and P. Bortolotti. Opportunities and challenges for spintronics in the microelectronics Industry. *Nature Electron* **2020**, 3, 446–459.
- [2] Atsufumi Hirohata; Keisuke Yamada; Yoshinobu Nakatani; Ioan Lucian Prejbeanu; Bernard Diény; Philipp Pirro and Burkard Hillebrands. Review on spintronics: Principles and device applications. *Journal of Magnetism and Magnetic Materials* **2020**, 509, 166711.
- [3] M. I. Dyakonov, and V.I. Perel. Current-induced spin orientation of electrons in Semiconductors. *Physics Letters A* **1971**, 35 (6), 459.
- [4] J. E. Hirsch. Spin Hall Effect. *Physical Review Letters* **1999**, 83, 1834.
- [5] Jairo Sinova; Sergio O. Valenzuela; J. Wunderlich; C. H. Back, and T. Jungwirth. Spin Hall Effects. *Reviews of Modern Physics* **2015**, 87, 1213.
- [6] Bychkov Yu. A.; Rashba E. I. Properties of a 2D electron gas with lifted spectral degeneracy. *JETP Letters* **1984**, vol. 39, issue 2, p. 66.

- [7] V.M. Edelstein. Spin polarization of conduction electrons induced by electric current in two-dimensional asymmetric electron systems. *Solid State Communications* **1990**, 73, 233–235.
- [8] J. C. Rojas Sánchez; L. Vila; G. Desfonds; S. Gambarelli; J. P. Attané; J. M. De Teresa; C. Magén and A. Fert. Spin-to-charge conversion using Rashba coupling at the interface between non-magnetic materials. *Nature Communications* **2013**, 4, 2944.
- [9] A. Manchon; H. C. Koo; J. Nitta; S. M. Frolov and R. A. Duine. New perspectives for Rashba spin–orbit coupling. *Nature Materials* **2015**, 14, 871–882.
- [10] Ioan Mihai Miron; Kevin Garello; Gilles Gaudin; Pierre-Jean Zermatten; Marius V Costache; Stéphane Auffret; Sébastien Bandiera; Bernard Rodmacq; Alain Schuhl; Pietro Gambardella. Perpendicular switching of a single ferromagnetic layer induced by in-plane current injection. *Nature* **2011**, vol. 476, no. 7359, pp. 189–193.
- [11] H. L. Wang, C. H. Du; Y. Pu; R. Adur; P. C. Hammel, and F. Y. Yang. Scaling of Spin Hall Angle in 3d, 4d, and 5d Metals from $Y_3Fe_5O_{12}$ /Metal Spin Pumping. *Physical Review Letters* **2014**, 112, 197201.
- [12] Qiming Shao; Peng Li; Luqiao Liu; Hyunsoo Yang; Shunsuke Fukami; Armin Razavi; Hao Wu; Kang Wang; Frank Freimuth; Yuriy Mokrousov; Mark D. Stiles; Satoru Emori; Axel Hoffmann; Johan Akerman; Kaushik Roy; Jian Ping Wang; See Hun Yang; Kevin Garello; Wei Zhang. Roadmap of Spin–Orbit Torques. *IEEE Transactions on Magnetism* **2021**, vol. 57, issue 7, 800439.
- [13] Hongyu An; Yuito Kageyama; Yusuke Kanno; Nagisa Enishi, and Kazuya Ando. Spin–torque generator engineered by natural oxidation of Cu. *Nature Communications* **2016**, 7, 13069.
- [14] K. Hasegawa; Y. Hibino; M. Suzuki; T. Koyama, and D. Chiba. Enhancement of spin-orbit torque by inserting CoO_x layer into Co/Pt interface. *Physical Review B* **2018**, 98, 020405.
- [15] Yuito Kageyama; Yuya Tazaki; Hongyu An; Takashi Harumoto; Tenghua Gao; Hi Shi, and Kazuya Ando. Spin-orbit torque manipulated by fine-tuning of oxygen-induced orbital hybridization. *Science Advances* **2019**, vol. 5, issue 11, eaax4278.
- [16] Junyeon Kim; Dongwook Go; Hanshen Tsai; Daegeun Jo; Kouta Kondou; Hyun-Woo Lee, and YoshiChika Otani. Nontrivial torque generation by orbital angular momentum injection in ferromagnetic-metal/Cu/ Al_2O_3 trilayers. *Physical Review B* **2021**, 103, L020407.

- [17] B. Andrei Bernevig; Taylor L. Hughes, and Shou-Cheng Zhang. Orbitronics: The Intrinsic Orbital Current in p-Doped Silicon. *Physical Review Letters* **2005**, 95, 066601.
- [18] H. Kontani; T. Tanaka; D. S. Hirashima; K. Yamada, and J. Inoue. Giant Orbital Hall Effect in Transition Metals: Origin of Large Spin and Anomalous Hall Effects. *Physical Review Letters* **2009**, 102, 016601.
- [19] Dongwook Go; Daegeun Jo; Changyoung Kim, and Hyun-Woo Lee. Intrinsic Spin and Orbital Hall Effects from Orbital Texture. *Physical Review Letters* **2018**, 121, 086602.
- [20] Daegeun Jo; Dongwook Go, and Hyun-Woo Lee. Gigantic intrinsic orbital Hall effects in weakly spin-orbit coupled metals. *Physical Review B* **2018**, 98, 214405.
- [21] Dongwook Go; Daegeun Jo; Hyun-Woo Lee; Mathias Kläui, and Yuriy Mokrousov. Orbitronics: Orbital currents in solids. *EPL* **2021**, 135 37001.
- [22] Seung Ryong Park; Choong H. Kim; Jaejun Yu; Jung Hoon Han, and Changyoung Kim. Orbital-Angular-Momentum Based Origin of Rashba-Type Surface Band Splitting. *Physical Review Letters* **2011**, 107, 156803.
- [23] Jin-Hong Park; Choong H. Kim; Hyun-Woo Lee, and Jung Hoon Han. Orbital chirality and Rashba interaction in magnetic bands *Physical Review B* **2013**, 87, 041301(R).
- [24] Jin-Hong Park; Choong H. Kim; Jun-Won Rhim, and Jung Hoon Han. Orbital Rashba effect and its detection by circular dichroism angle-resolved photoemission spectroscopy. *Physical Review B* **2012**, 85, 195401.
- [25] Dongwook Go and Hyun-Woo Lee. Orbital torque: Torque generation by orbital current injection. *Physical Review Research* **2020**, 2, 013177.
- [26] Dongwook Go; Jan-Philipp Hanke; Patrick M. Buhl; Frank Freimuth; Gustav Bihlmayer; Hyun-Woo Lee; Yuriy Mokrousov, and Stefan Blügel. Toward surface orbitronics: giant orbital magnetism from the orbital Rashba effect at the surface of sp-metals. *Scientific Reports* **2017**, 7:46742.
- [27] Dongwook Go; Daegeun Jo; Tenghua Gao; Kazuya Ando; Stefan Blügel; Hyun-Woo Lee, and Yuriy Mokrousov. Orbital Rashba effect in a surface-oxidized Cu film. *Physical Review B* **2021**, 103, L121113.
- [28] Leandro Salemi; Marco Berritta; Ashis K. Nandy, and Peter M. Oppeneer. Orbitaly dominated Rashba-Edelstein effect in noncentrosymmetric antiferromagnets. *Nature Communications* **2019**, 10, 5381.

- [29] Shilei Ding; Andrew Ross; Dongwook Go; Lorenzo Baldrati; Zengyao Ren; Frank Freimuth; Sven Becker; Fabian Kammerbauer; Jinbo Yang; Gerhard Jakob; Yuriy Mokrousov, and Mathias Kläui. Harnessing Orbital-to-Spin Conversion of Interfacial Orbital Currents for Efficient Spin-Orbit Torques. *Physical Review Letters* **2020**, 125, 177201.
- [30] Yuya Tazaki; Yuito Kageyama; Hiroki Hayashi; Takashi Harumoto; Tenghua Gao; Ji Shi, and Kazuya Ando. Current-induced torque originating from orbital current. *arXiv* **2019**, 2004.09165.
- [31] Genki Okano; Mamoru Matsuo; Yuichi Ohnuma; Sadamichi Maekawa, and Yukio Nozaki. Nonreciprocal Spin Current Generation in Surface-Oxidized Copper Films. *Physical Review Letters* **2019**, 122, 217701.
- [32] See Supplemental Material for the description of the samples preparation, FMR characterization and details of the spin current generation and detection.
- [33] Amare Aregahegn Dubale; Chun-Jern Pan; Andebet Gedamu Tamirat; Hung-Ming Chen; Wei-Nien Su; Ching-Hsiang Chen; John Rick; Delele Worku Ayele; Belete Asefa Aragaw; Jyh-Fu Lee; Yaw-Wen Yang, and Bing-Joe Hwang. Heterostructured Cu₂O/CuO decorated with nickel as a highly efficient photocathode for photoelectrochemical water reduction. *Journal of Materials Chemistry A* **2015**, 3, 12482-12499.
- [34] Yaroslav Tserkovnyak; Arne Brataas, and Gerrit E. W. Bauer. Enhanced Gilbert Damping in Thin Ferromagnetic Films. *Physical Review Letters* **2002**, 88, 117601.
- [35] A. Azevedo; L. H. Vilela-Leão; R. L. Rodríguez-Suárez; A. F. Lacerda Santos, and S. M. Rezende. Spin pumping and anisotropic magnetoresistance voltages in magnetic bilayers: Theory and experiment. *Physical Review B* **2011**, 83, 144402.
- [36] K. Uchida; S. Takahashi; K. Harii; J. Ieda; W. Koshibae; K. Ando; S. Maekawa, and E. Saitoh. Observation of the spin Seebeck effect. *Nature* **2008**, 455, 778–781.
- [37] S. M. Rezende; R. L. Rodríguez-Suárez; R. O. Cunha; A. R. Rodrigues; F. L. A. Machado; G. A. Fonseca Guerra; J. C. Lopez Ortiz, and A. Azevedo. Magnon spin-current theory for the longitudinal spin-Seebeck effect *Physical Review B* **2014**, 89, 014416.
- [38] Kuntal Roy. Estimating the spin diffusion length and the spin Hall angle from spin pumping induced inverse spin Hall voltages. *Physical Review B* **2017**, 96, 174432.
- [39] Luqiao Liu; R. A. Buhrman, and D. C. Ralph. Review and Analysis of Measurements of the Spin Hall Effect in Platinum. *arXiv* **2011**, 1111.3702.

